Sanroman-Junquera, M.; Mora-Jimenez, I.; Garcia-Alberola, A.; Caamano, AJ.; Trenor Gomis, BA.; Rojo-Alvarez, JL. (2018). Arrhythmia Mechanism and Scaling Effect on the Spectral Properties of Electroanatomical Maps with Manifold Harmonics. IEEE Transactions on Biomedical Engineering (Online). 65(4):723-732. doi:10.1109/TBME.2017.2716189

Arrhythmia Mechanism and Scaling Effect on the Spectral Properties of Electroanatomical Maps With Manifold Harmonics

Margarita Sanromán-Junquera[1], Inmaculada Mora-Jiménez[1], Arcadio García-Alberola[2], Antonio Caamaño[1], Beatriz Trenor[3], José Luis Rojo-Álvarez[1]

Affiliations: [1] Department of Signal Theory and Communications, Telematics and Computing, Universidad Rey Juan Carlos, Fuenlabrada Madrid, Spain

[2] Arrhythmia Unit, Hospital Universitario Virgen de la Arrixaca, Murcia, Spain

[3] I3BH - Universitat Politècnica de València, Valencia, Spain

Correspondence: Margarita Sanromán-Junquera D-207, Departamental III, Universidad Rey Juan Carlos, c/Camino del molino s/n, 28943, Fuenlabrada, Madrid Spain.
e-mail: margarita.sanroman@urjc.es

Abstract

Spatial and temporal processing of intracardiac electrograms provides relevant information to support the arrhythmia ablation during electrophysiological studies. Current Cardiac Navigation Systems (CNS) and Electrocardiographic Imaging (ECGI) build detailed three dimensional electroanatomical maps (EAM), which represent the spatial anatomical distribution of bioelectrical features, such as activation time or voltage amplitude. We present a principled methodology for spectral analysis of both EAM geometry and bioelectrical feature in CNS or ECGI, including their spectral representation, cut-off frequency, or spatial sampling rate (SSR). Existing manifold harmonic techniques for spectral mesh analysis are adapted to account for a fourth dimension, corresponding to the EAM bioelectrical feature. Scaling is required to address different magnitudes and units. With our approach, simulated and real EAM showed strong SSR dependence on both the arrhythmia mechanism and the cardiac anatomical shape. For instance, high frequencies increased significantly the SSR since the early-meets-late in flutter EAM, compared to the sinus rhythm. Besides, higher frequencies components were obtained for left atrium (more complex anatomy) than for right atrium in sinus rhythm. The proposed manifold harmonics methodology opens the field towards new signal processing tools for principled EAM spatio-feature analysis in CNS and ECGI, and to an improved knowledge on arrhythmia mechanisms.

Keywords: Cardiac Navigation System, Spectral Analysis, Bandwidth, Spatial Sampling Rate, Electrophysiological Study, Electrocardiographic Imaging.

1 Introduction

Electric potential measurements inside the heart, so-called electrograms (EGM), are used to support clinicians in the treatment of cardiac arrhythmias during the electrophysiological studies (EPS). The knowledge of the precise position of each EGM can help to apply the therapy, usually cardiac ablation, in a more effective way. Given that there is no medical image modality allowing the clinician to visualize the three-dimensional (3D) cardiac bioelectricity, several technologies have been proposed for this end, namely, cardiac navigation systems (CNS) or Electrocardiographic Imaging (ECGI).[4,10] In both types of systems, a mesh of the cardiac chamber surface is first built to visualize its anatomical shape, and then to provide a 3D electroanatomical map (EAM) of a bioelectrical feature of interest (such as activation time, or voltage amplitude). The anatomical mesh is composed by a set of vertices in the 3D space joined by triangular faces. The bioelectrical feature is also associated to each vertex as an additional dimension.

Until recently, CNS allowed to build the EAM by sequentially registering EGMs and their corresponding anatomical positions in the cardiac endocardium, and then a basic interpolation was used to help in the EAM visualization. However, the most recent CNS use multielectrode catheters and fast acquisition of a much higher number of electroanatomical samples, which are subsequently filtered to provide sets of quality signals[1,14]. Current ECGI systems also supply with large number of virtual EGMs on the epicardium compared to traditional CNS.[10] As far as we are today working with several thousands of anatomically recorded EGMs, there is a need for moving from heuristically based information processing procedures to advanced and principled algorithms allowing to handle the redundancy and spatio-temporal correlations from currently available cardiac bioelectric measurements.

While Fourier analysis (FA) has been often used as a well-founded technique for frequency domain analysis in uniformly sampled spaces,[6] a variety of mesh Laplacian operators have been proposed as an approximation of the Fourier Transform (TF) on 2-manifold surfaces.[18] Among these Laplacian operators, this work uses the discrete Laplacian operator based on Manifold Harmonics Analysis (MHA) proposed by Vallet and Lévy.[17] We considered

triangle meshes of EAM as closed 2-manifolds. Spectral analysis has been highly informative about cardiac arrhythmia mechanism from ECG and EGM time signals, however, there is no principled theory suitable for handling basic concepts of spectral analysis in EAM embedded in 2-manifolds.[2]

A simple methodology for spectral processing in 2-manifolds was introduced to provide useful quantitative magnitudes and qualitative comparison, such as bandwidth, spectral content, or frequency bands, from EAM and anatomical meshes usually obtained in current CNS and ECGI systems.[12,13] In these preceding works, a simple, yet theoretically well principled method was presented for EAM spectrum representation from MHA. Nevertheless, little attention has been paid to the issue of different order of magnitudes and units among anatomical and physiological features (such as mV for voltage amplitude maps, or ms for activation maps). As far as the matrix operations involved in MHA are related to eigendecomposition operators working on mixed measurements, their different orders of magnitude and units can be expected to have noticeable impact on the spectral magnitudes estimated with this technique.

Therefore, our first objective in the present work was to analyze and provide with clear guidelines when using MHA for spectral analysis of EAM in CNS and ECGI. A preliminary study of the anatomical and electrical feature scaling effects was recently presented,[11] whose results are here extended by evaluating two more types of scaling and also assessing the impact of the scaling in the EAM spectral properties. On the other hand, and taking into account that cardiac bioelectric activity is strongly linked and dependent on the underlying arrhythmic mechanism, we also scrutinized the impact of different arrhythmia mechanisms on EAM by using the Spatial Sampling Rate (SSR) to know its potential usefulness defining the number of required anatomical samples during CNS or the resolution attainable in ECGI systems. With this same purpose, we also studied the spatial smoothness on the anatomical and EAM spectrum (low-pass filtered EAM), in a similar way that one-dimensional spectral analysis provides operative and well-defined quantitative criteria to analyze the smoothness in one-dimensional cardiac signals. For all these analyses, we used three sets of data: (1) a

simple and synthetic tear-shaped mesh example with a feature projected on it; (2) detailed simulations of both temporal series of potential EAM during an atrial sinus tachycardia (AT) and atrial fibrillation (AF), and activation time EAM during a sinus rhythm (SR) and a flutter arrhythmia (FL) in both atria; (3) a set of real EAM registered in the left atrium (LA), left ventricle (LV), and right ventricle (RV) of patients undergoing therapy supported with CNS.

The rest of the paper is structured as follows. In the next section, we summarize the theoretical framework of MHA for 2-manifolds, and its extension for spectral analysis in EAM that are usually informative in the setting of EPS and cardiac arrhythmia ablation support. In Section 3, spectral representation and analysis, SSR, and EAM reconstruction are assessed for simulated and real EAMs. Finally, in Section 4, discussion and conclusions are summarized.

2 Materials and Methods

A summary explanation of the theoretical framework for MHA and its computation is first presented. Then, a new and simple methodology is proposed to estimate the spectral representation of EAMs, and to establish a cut-off frequency to determine the SSR according to the quality of the reconstructed EAM. Finally, the need of a scaling is pointed out when different orders of magnitudes and units are mixed in the definition of the vertex coordinates.

2.1 Manifold Harmonics

Although the traditional spectral analysis is based on the FA, the FT of a signal cannot be directly applied to manifold with arbitrary topology.[15] The classical FT uses a fixed set of basis functions, and it can be seen as a linear combination of the Laplace Operator eigenvectors.[15] However, the eigenvectors, which represent the Fourier basis for manifold meshes, are dependent on the mesh topology.

Among the different approaches proposed to define the Laplacian in a manifold,[18] the

discrete Laplacian operator (or geometric Laplacian) takes into account not only the connectivity between vertices, but also the manifold geometry. Let be $\boldsymbol{f}$ a twice-differentiable real-valued function, then the Laplacian of $\boldsymbol{f}$ is defined by the divergence of its gradient as:

$$\Delta \boldsymbol{f} = \text{div}(\text{ grad } \boldsymbol{f}) = \nabla \cdot \nabla \boldsymbol{f} \tag{1}$$

The Laplace-Beltrami operator (LBO) allows to extend the Laplacian to the function $\boldsymbol{f}$ defined over a Riemannian or pseudo-Reimannian manifolds with metric $\boldsymbol{g}$ as:[9]

$$\Delta \boldsymbol{f} = \sum_i \frac{1}{\sqrt{|\boldsymbol{g}|}} \delta_i \left(\sqrt{|\boldsymbol{g}|} \sum_j \boldsymbol{g}^{ij} \delta_j \boldsymbol{f} \right) \tag{2}$$

where δ_i denotes differentiation with respect to the i-th coordinate function, $|\boldsymbol{g}|$ is the determinant of $\boldsymbol{g}$, and $\boldsymbol{g}^{ij}$ is the (i, j) component of the inverse of $\boldsymbol{g}$.[5] The discrete exterior calculus simplifies the calculations of the LBO on manifolds by defining the Laplace-de Rham operator (LRO), which is equivalent to LBO for functions on a manifold (0-forms).[19] Following the approach proposed by Vallet et Lévy,[17] the LRO, $\boldsymbol{\Delta}$, is defined as:

$$\boldsymbol{\Delta}_{ij} = \begin{cases} -\frac{cotan(\beta_{ij}) + cotan(\alpha_{ij})}{\sqrt{|\boldsymbol{v}_i||\boldsymbol{v}_j|}} & \text{if } i \neq j \\ -\sum_{k \in N(\boldsymbol{v}_i)} \boldsymbol{\Delta}_{ik} & \text{if } i = j \end{cases} \tag{3}$$

where $\boldsymbol{\Delta}$, is a $n \times n$ matrix, where n is the number of vertices; $\boldsymbol{v}_i = (x_i, y_i, z_i)$ and $\boldsymbol{v}_j = (x_j, y_j, z_j)$ are spatial vertices linked by an edge; β_{ij} and α_{ij} are the opposite angles to the edge between $\boldsymbol{v}_i$ and $\boldsymbol{v}_j$; $N(\boldsymbol{v}_i)$ is the 1-ring first-order neighbors of $\boldsymbol{v}_i$; and $|\boldsymbol{v}_i|$ is the area of the Voronoi region of the vertex $\boldsymbol{v}_i$ in its 1-ring neighbor.[7] This LRO uses a symmetrized cotangent scheme to have positive eigenvalues and orthogonal eigenvectors.[8]

The eigenfunctions of the Laplace operator on a manifold, so-called Manifold Harmonics, define the eigenvectors and eigenvalues $\{\boldsymbol{H}^k, \lambda^k\}$ that satisfy

$$-\boldsymbol{\Delta} \boldsymbol{H}^k = \lambda_k \boldsymbol{H}^k \tag{4}$$

where $k = (1, \ldots, n)$, $\boldsymbol{H}^k$ are an orthonormal basis (*Manifold Harmonic Basis*, MHB), and the eigenvalues λ_k are directly related to the spatial frequency as $w_k \approx \sqrt{\lambda_k}$, and inversely to

the edge length[17]. Lower (higher) eigenvalues λ_k correspond to lower (higher) frequencies, and hence, longer (shorter) edges.

The Manifold Harmonic Transform (MHT) projects the coordinates of the vertices onto the orthonormal basis ($\boldsymbol{H}^k$), hence transforming the the spatial domain into a frequency domain. The vertices projections are called *spectral coefficients* and they can be computed as $\hat{\boldsymbol{a}}_k = \sum_{i=1}^{n} \boldsymbol{v}_i \boldsymbol{H}_i^k$. The reconstruction of the original mesh can be obtained by computing the inverse of MHT as

$$\hat{\boldsymbol{v}}_i = \sum_{k=1}^{m} \hat{\boldsymbol{a}}_k \boldsymbol{H}_i^k \tag{5}$$

where m is the number of coefficients used for reconstruction. As lower eigenvalues (and their associated eigenvectors) correspond to the general shape of the mesh (lower frequencies), a low-pass filtered shape of the mesh is obtained for $m << n$. The original mesh is reconstructed when $m = n$.[17]

To our knowledge, the decision of the number of lower frequency bands, i.e. cut-off frequency, and hence the suitable SSR to provide appropriate spatial sampling criterion according to the Nyquist limit, has been mostly done to date in terms of heuristics, rather than in terms of spectral quantitative criteria.

2.2 SSR Estimation With MHA

We proposed a method to estimate the SSR in cardiac EAMs by extending the previously described MHA. For this purpose, and given that the methodology defined in Section 2.1 only takes into account the geometry (anatomy) to obtain the mesh spectrum, we extended the MHA formulation up to the fourth dimension, corresponding to the cardiac feature in EAMs.

Following the formulation proposed by Vallet et Lévy,[17] the couple $\{\boldsymbol{H}^{ke}, \lambda_{ke}\}$ is obtained now by computing the eigenfunctions of Eq. (3), but vertices are now defined as $\boldsymbol{u} = (x, y, z, h)$, where h is the cardiac feature (such as activation time, unipolar or bipolar voltage amplitude) measured at vertex with Cartesian coordinates (x, y, z). The new $\boldsymbol{\Delta}^e$ matrix is now defined

as:

$$\boldsymbol{\Delta}_{ij}^{e} = \begin{cases} -\frac{cotan(\beta_{ij})+cotan(\alpha_{ij})}{\sqrt{|\boldsymbol{u}_i||\boldsymbol{u}_j|}} & \text{if } i \neq j \\ -\sum_{k \in N(\boldsymbol{u}_i)} \boldsymbol{\Delta}_{ik}^{e} & \text{if } i = j \end{cases} \tag{6}$$

where $\boldsymbol{u}_i = (x_i, y_i, z_i, h_i)$ and $\boldsymbol{u}_j = (x_j, y_j, z_j, h_j)$ are vertices linked by an edge; β_{ij} and α_{ij} are the opposite angles to the edge between $\boldsymbol{u}_i$ and $\boldsymbol{u}_j$; $N(\boldsymbol{u}_i)$ is the 1-ring first-order neighbors of $\boldsymbol{u}_i$; and $|\boldsymbol{u}_i|$ is the area of the Voronoi region of the vertex $\boldsymbol{u}_i$ in its 1-ring neighborhood.

Once the MHT is computed, and spectral coefficients $\hat{\boldsymbol{a}}_{ke}$ are obtained for both anatomy and EAM features, the steps for estimating the SSR are the following:

1. Compute n EAM reconstructions by gradually increasing m from 1 to n in Eq. (5). The larger m, the better similarity between reconstructed and original EAMs, which can be quantified by the accumulated normalized correlation coefficient (ANCC) for each j-th element of $\boldsymbol{u}$, as follows,

$$C_j(w_m) = \frac{cov(\hat{\boldsymbol{u}}_m^j, \boldsymbol{u}^j)}{\sqrt{var(\hat{\boldsymbol{u}}_m^j)var(\boldsymbol{u}^j)}} \tag{7}$$

   where *cov* and *var* denote covariance and variance, respectively; j corresponds to each dimension, i.e. x, y, z, and h; m is the number of components considered for the reconstruction; $\hat{\boldsymbol{u}}_m^j$ is the j-th element of $\hat{\boldsymbol{u}}_m$ in Eq. (5); and $\boldsymbol{u}^j$ is the j-th element of the original vertices. $C_j(w_m)$ allows us to quantify the quality of the reconstructed EAM.

2. Select the cut-off frecuency w_c such that ANCC for all dimensions exceeds certain threshold. This value will be denoted from now on as C_{w_c}.

   The cut-off frequency encompasses the lowest spectrum components providing the general shape of the EAM. The threshold represents a quality measurement of the reconstructed EAMs. This quality will be strongly dependent on the application.

3. Obtain the edge length L for the selected w_c, given by $L = 1/w_c = 1/\sqrt{\lambda_c}$.

4. By assuming the mesh is composed of equilateral triangular faces of edge length L, obtain the triangle area as $A_t = \sqrt{3} \cdot L^2/4$. Since the number of faces is approximately twice the number of vertices, the SSR can be estimated by

$$SSR \approx \frac{A_T}{2 \cdot A_t} \tag{8}$$

where A_T is the total surface area obtained as the sum of all original face areas. The use of SSR throughout the paper was chosen for giving a consistent measurement for the bandwidth. In other words, rather than using w_c, which includes mixed nature physical units (spatial and feature), the SSR give an idea on the number of spectral samples to be measured for the description of the changes in the EAM.

Note that the assumption of equilateral is a simplification for giving an operative numerical approximation. The hypothesis of equilateral triangular faces will certainly result in a SSR higher than the original number of vertices when the EAM has a great variation of the edge-lengths. The higher the number of vertices, the best this hypothesis will be accomplished.

In addition, a normalized spectrum is computed to have a representation valid for comparing the spectrum of different EAMs. The EAM spectrum for the j-th element of $\boldsymbol{u}$ is computed through the normalized correlation coefficient (NCC) S_j between the j-th element of original vertices $\boldsymbol{u}$ and $\tilde{\boldsymbol{u}}_k = \hat{\boldsymbol{a}}_{ke}\boldsymbol{H}^{ke}$ (projection of each spectral coefficient in its MHB), i.e.,

$$S_j(w_k) = \frac{cov(\tilde{\boldsymbol{u}}_k^j, \boldsymbol{u}^j)}{\sqrt{var(\tilde{\boldsymbol{u}}_k^j) var(\boldsymbol{u}^j)}} \tag{9}$$

The frequency associated to the k-th eigenvector is given by w_k. Note that S_j is a normalized version of the $|\hat{\boldsymbol{a}}_{ke}|$ coefficients.

In this new approach, different orders of magnitudes and units are mixed, such as, length units for the geometry and voltage or time units for the feature in EAMs. Therefore, it makes necessary to scale the vector $\boldsymbol{u}$ to reduce the impact of a dominant dimension in the calculation of the eigenvectors and eigenvalues of $\boldsymbol{\Delta}$ matrix.

[Figure 1 about here.]

Figure 1 shows an example of the different orders of magnitude effect in a synthetic tear-shaped mesh. Figure 1 (a) represents a tear-shaped mesh, and its flatted version, as a result of dividing the z-coordinate by 1321 (random number). Figure 1 (c) and (d) show the spectra of the tear-shaped mesh and the flatted version, respectively. Vertical lines establish the required w_c to have the $C(w_c)$ value marked with the corresponding arrow. Note that the spectral profile has a marked low-pass character, hence higher correlations were obtained for low frequencies. However, the w_c is significant higher for the flatted mesh due to the w is inversely related to the length of the edges and the flatted tear-shaped mesh has shorter edges. This effect has a direct consequence in the SSR, for instance, meanwhile $w_c \approx 0.25$ and $SSR = 237$ for $C(w_c) = 0.99$ in the original mesh, $w_c \approx 2$ and $SSR = 7032$ in the flatted mesh. Figure 1 (d) shows the reconstruction of both meshes (the flatted tear-shaped mesh was re-sized after reconstruction) using $C(w_c) \approx 0.95$, $C(w_c) \approx 0.99$, $C(w_c) \approx 0.999$. The reconstruction of the flatted tear-shaped mesh has clearly lower quality than the original one.

This procedure can be now readily applied for analyzing EAMs in CNSs, as far as they are a collection of vertices and faces with associated electrical information.

3 Results

A set of experiments are next presented to calculate the spectra, and suitable values of SSR on EAMs with the proposed MHA-based methodology in different datasets. In this section, different scalings are assessed in order to select the most appropriate one for the spectral analysis. Then, we present the materials (simulated and real EAMs). Finally, the SSRs, the spectra, and the EAM reconstructions are computed for simulated and real EAMs, which include both anatomy (geometry) and features, during different heart rhythms.

3.1 Databases for SSR Validation

Different databases have been used for validation of the proposed methodology in selected case studies. The SSR was first obtained in simulated EAMs: two activation time EAMs in

a SR, and a FL, and a temporal series of potentials EAMs in an AT and AF arrhythmia[3]. Simulations were provided by a model of the atria (right and left), composed of a set of nodes simulating the cardiac electric propagation[16]. All nodes were used as vertices in a mesh, and a cardiac feature (time activation) was associated to each vertex by processing the EGM registered at each node. Time activation was obtained by taking a vertex as a reference and computing the time difference between the maximum deflection of each EGM and the maximum deflection of reference EGM in a window of interest (beat length). The potentials were obtained by taking the maximum voltage at each vertex for different time instants. The right (left) atrial mesh was composed by 18183 (21538) vertices. Finally, real bipolar voltage amplitude and activation time EAMs from CNS (Carto®, Biosense Webster) from patients referred to EPS, were also analyzed in this section. These EAMs belong to 1 LA, 4 LVs, and 4 RVs, and they were composed by 1464.5 ± 971.9 vertices (mean $\pm$ standard deviation).

3.2 Evaluation of Scaling

We analyzed the effect of different scaling schemes in the spectrum, EAM reconstruction, and SSR when different orders of magnitudes and units are mixed in the coordinates of the EAM vertices. Previous to the scaling, every dimension was centred to have zero mean value. Specifically, we evaluated three scalings: **S1**, unit standard deviation for each dimension; **SMG**, the same standard deviation for each dimension, obtained as the average of the standard deviation of all dimensions; **SH**, just scaling the feature dimension with the average of ratio between every spatial dimension (x, y, and z) and the feature dimension. Although, this last scaling focused on the feature dimension (different units and probably orders of magnitudes), it can be used to scale other dimensions by just changing the feature dimension with the dimension to scale.

[Figure 2 about here.]

First, we evaluated the scaling in the flatted tear-shaped mesh (Figure 1 (a)) presented in the previous section. Figures 2 (a), (b), and (c) show the spectrum and the corresponding w_c

for three different $C(w_c)$ (0.95, 0.99, and 0.999) applying the S1, SMG, and SH scaling to the flatted tear-shape mesh, respectively. Note that the cut-off frequencies for SMG and SH scalings were quite similar to the original one (see Figure 1 (c)); however, the shapes of the spectra were quite different due to the scaling modified the spectrum of all dimensions. The spectrum with S1 scaling had the same shape as the spectrum with SMG scaling, but w_c was higher for the same $C(w_c)$. This effect was a consequence of the smaller size of the S1 scaling mesh, hence, the length of the edges and the w_c were also smaller and higher, respectively. Figure 2 (d) shows the reconstruction for $C(w_c) \approx 0.95$, $C(w_c) \approx 0.99$, and $C(w_c) \approx 0.999$ with S1, SMG, and SH scaling. Note that the scaling was reverted and the z-coordinate was re-sized in these reconstructions for comparison purposes. While similar reconstructions were obtained with S1 and SMG scalings, lower quality reconstruction was yielded for SH scaling.

[Figure 3 about here.]

In the next example, a feature was projected above the surface of the tear-shaped mesh in order to simulate a EAM. This feature mimicked two foci of activation in a cardiac chamber (see the first EAM in Figure 3 (f)). Figures 3 (a)-(d) shows the spectra of the 2-foci-EAM without scaling (a), with S1 (b), with SMG (c), and with SH (d) scalings. The spectral shapes of S1 and SMG scalings were similar; the spectrum with S1 scaling was wider than the spectrum with SMG due to the lower size of the S1 scaled EAM. For $C(w_c) \approx 0.99$, the w_c was higher for the non-scaled spectrum than SMG and sh scaled spectra. As a consequence, the non-scaled EAM yielded a extremely higher SSR (values of 8500 for a $C(w_c) \approx 1$ when this mesh had 1000 vertices) as shown in Figure 3 (e). Considering the black horizontal line in the zoom part of Figure 3 (e), $C(w_c) \approx 0.609$ for a $SSR = 167$ in the non-scaled EAM, $C(w_c) = 0.978$ for a $SSR = 145$ in the S1 and SMG scaled EAM, and $C(w_c) = 0.94$ for a $SSR = 150$ in the SH scaled EAM. These results showed that better quality of the reconstructed EAM was obtained using few vertices with the S1 or SMG scalings. For the previous SSR values, Figure 3 (f) shows the original EAM and the reconstructed EAM without scaling, and with S1, SMG, and SH scaling. Higher quality meshes were also illustrated

in the reconstruction with S1 and SMG scalings. The SH scaled reconstructed EAM had a significant lower number of components, this reconstruction considered $C(w_c) = 0.923$, resulting a $SSR = 96$; the addition of one extra component increased the SSR to 206. Therefore, S1 or SMG scaling seems to be the best approach to estimate the SSR in EAM. In the following, the SMG scaling will be considered in results and figures.

3.3 SSR Estimation for Simulated EAMs

SSR of detailed simulated EAMs were estimated for both anatomy and features by using the MHA-based methodology, specifically, two activation time EAMs for both atria during simulated SR and FL, and a temporal series of potential EAMs for the LA during simulated AT and AF.

[Figure 4 about here.]

EAM were transformed into a spatial frequency space by computing the MHT, and the SSR was estimated using the proposed methodology. Figure 4 (a)-(d) shows the spectrum associated to time activation EAM for a SR in the RA (a) and the LA (b), and for a FL in the RA (c) and the LA (d). For the LA, the projected feature changed smoothly in both SR and FL (the electric wavefront was spread through the atrium in a normal pattern, faster for the FL), hence, similar w_c was obtained in both rhythms. On the contrary, the wavefront was rotating around the right atrial valve in the FL and generating step boundaries in cyclic representations of the EAM. This phenomenon is known as *early-meets-late* and it produced a more widespread spectrum due to the fast variations of the feature (high frequencies). Although the feature varied also smoothly in the RA for the SR, a difference of the w_c was obtained for SR due to the higher complexity of the LA anatomy (considering that veins introduce high frequencies). These differences in w_c are clearer shown in Figure 5 (e), where the highest values of SSR were required for FL in the RA, meanwhile the lowest SSRs were required for the SR in the RA. For LA, both rhythms needed similar values of SSR. For

example, for a $C(w_c) \approx 0.99$, the SSRs were 207 in the RA and 267 in the LA for SR and, 247 in the LA, and 357 in the RA for the FL.

[Figure 5 about here.]

Figures 5 (b)-(e) show the original (upper panels) and the reconstruction (bottom panels) of the time activation EAMs in the RA (b) and the LA (c) for a SR, and in the RA (d) and the LA (e) for the FL with $C(w_c) \approx 0.99$. Reconstructions showed that the veins were partially removed due to the high frequencies at their borders; however, the feature was reconstructed with a high quality, and the *early-meets-late* was clearly represented in the FL of the RA, which showed the direction of the electrical impulse movement.

[Figure 6 about here.]

Figure 6 (a) shows the two faces of a temporal series of potential EAMs in the LA during AT. The sequence had a duration 300 miliseconds (ms) and the snapshots were taken each 50 ms. Figure 6 (b) shows the SSR for different $C(w_c)$ in the LA during the AT. The pair of time instants $t_0 + 100$ ms and $t_0 + 300$ ms had similar values of SSRs due to they had similar patterns of potential maps. The time instants $t_0 + 50$ ms and $t_0 + 250$ ms also had similar patterns of potential map and SSRs; however, SSRs were lower than for $t_0 + 100$ ms and $t_0 + 300$ ms because the EAMs for $t_0 + 50$ ms and $t_0 + 250$ ms were smoother. Finally, the lowest SSR values were for t_0 ms, $t_0 + 150$ ms, and $t_0 + 200$ ms, whose EAMs were the smoothest. Figure 6 (b) shows the two faces of the temporal series of reconstructed potential EAMs in the LA during AT using $C(w_c) \approx 0.99$. Reconstructions showed a high quality propagation patterns of the electrical wavefront, although the veins were partially removed (high frequencies). SSRs were 1251 for $t_0 + 100$ ms, 1193 for $t_0 + 300$ ms, 776 for $t_0 + 250$ ms, 573 for $t_0 + 50$ ms, 313 for $t_0 + 200$ ms, 296 for $t_0 + 150$ ms, and 292 for t_0 ms, which corresponded to the complexity of the potential map: the higher EAM complexity, the higher SSRs.

[Figure 7 about here.]

Figure 7 (a) shows the two faces of the temporal series of potential EAM in the LA during AF. The sequence has a duration of 300 miliseconds and the snapshots are taken each 20 ms. Note that AF is a faster rhythm than AT. The simulated AF consisted of a rotor, i.e. rotational activation, in the LA wall. Figure 7 (c) shows the SSR for the temporal series of potential EAM in AF. The complexity of AF in the LA is shown in all EAMs (in both anatomy and feature), and consequently no high differences exist between the different EAMs. Figure 7 (b) shows the two faces of the temporal series of reconstructed with $C(w_c) \approx 0.99$ potential EAMs in the LA during AF. As previous reconstructions, the borders of the pulmonary veins were also partially removed, although the wavefront patterns of the rotor in the reconstructed EAMs were completely recovered. SSRs for $C(w_c) \approx 0.99$ were from 1000 to 2000 samples, higher values than SSRs in AT, FL, and RS EAMs due to more complex arrhythmia mechanism in AF. Note that the cut-off frequency, and hence, the SSR are dependent on the arrhythmia dynamic or the electric substrate.

3.4 SSR Estimation for Real EAMs from CNS

Real bipolar voltage amplitude and time activation CNS EAMs of 1 LA 4 LVs, and 4 RVs were analysed by following the proposed methodology. Table 1 shows the SSR for $C(w_c) \approx 0.99$, $C(w_c) \approx 0.95$, and $C(w_c) \approx 0.90$. The SSR was very dependent on the type of EAM, for example, meanwhile the SSR for AI was 292 when $C(w_c) \approx 0.99$, the SSR for VI-1 was 1647. The explanation to this example is shown in Figures 8 (a) and (b), which represent the spectra of both EAMs. The spectrum of LV-1 EAM was more spread than that of LA EAM, likely due to the higher variation of the feature in the first one (see Figure 8 (c)). However, the required w_c and SSR could be different according to the specific EAM, for example, in this case, the w_c of activation time EAM of LV-1 was higher than the bipolar one (SSR = 1647 for activation time EAM, SSR = 352 for bipolar voltage EAM), meanwhile it was the opposite for the LA (SSR = 292 for activation time EAM, SSR = 845 for bipolar voltage EAM) .

[Figure 8 about here.]

[Table 1 about here.]

4 Discussion

A simple methodology based on MHA has been proposed for spectral analysis of detailed EAM provided by CNS and ECGI. Existing MHA formulations were only defined for 2-manifold, and we have extended this definition for its usefulness in EAM, which include not only anatomical information but also a cardiac bioelectrical feature measured at each vertex. When analyzing simulated activation time EAMs, FL in the RA apparently required a higher SSR due to the *early-meets-late* phenomenon, which generates high variation of the feature (high frequencies). On the other hand, activation time EAM in the RA required similar SSR during SR and FL due to the smooth variation of the feature in the EAM. Higher complexity in the propagation pattern, such as rotors in FA, required higher SSRs. For real EAMs, the SSR was very dependent on the arrhythmia mechanism and the type of the EAM (bipolar or activation time).

Several limitations can be pointed in the proposed methodology. Only some representative case studies (namely, 2 simulated activation time EAMs, a temporal series of potential EAMs, and 9 CNS EAM) have been used here for validation purposes. However, the actual benefit for the clinical practice will be supported by extended studies for different arrhythmias in simulated and real EAM in CNS. The SSR was estimated with the underlying assumption of uniform spatial sampling for yielding the edge length as a summary result for a given chamber (equilateral triangular faces), which is only a valid assumption for a large enough number of vertices. However, both current CNS and ECGI are very densely sampled, hence the assumption would be achieved in most of the cases.

The proposed MHA methodology opens the field towards a new set of fundamental tools for principled spatio-feature spectral analysis of EAM and improved knowledge on arrhythmia mechanisms.

Conflict of Interest

The authors have declared that no competing interests exist.

Acknowledgment

This work has been partly supported by Spanish Research Projects TEC2013-48439-C4-1-R and TEC2016-75161-C2-1-4.

References

1. Anter, E., T. H. McElderry, F. M. Contreras-Valdes, J. Li, P. Tung, E. Leshem, C. I. Haffajee, H. Nakagawa, and M. E. Josephson. Evaluation of a novel high-resolution mapping technology for ablation of recurrent scar-related atrial tachycardias. Heart Rhythm, 2016.

2. Barquero-Pérez, O., J. Rojo-Álvarez, A. Caamaño, R. Goya-Esteban, E. Everss, F. Alonso-Atienza, J. Sánchez-Muñoz, and A. García-Alberola. Fundamental frequency and regularity of cardiac electrograms with fourier organization analysis. IEEE Transactions on Biomedical Engineering 57:2168–2177, 2010.

3. Dux-Santoy, L., R. Sebastian, J. Felix-Rodriguez, J. Ferrero, and J. Saiz. Interaction of specialized cardiac conduction system with antiarrhythmic drugs: a simulation study. IEEE Transactions on Biomedical Engineering 58:3475–8, 2011.

4. Luther, V., N. W. Linton, S. Jamil-Copley, M. Koa-Wing, P. B. Lim, N. Qureshi, F. S. Ng, S. Hayat, Z. Whinnett, D. W. Davies *et al.* A prospective study of ripple mapping the post-infarct ventricular scar to guide substrate ablation for ventricular tachycardia. Circulation: Arrhythmia and Electrophysiology 9:e004072, 2016.

5. Mahadevan, S. Representation Discovery using Harmonic Analysis, Morgan and Claypool Publishers, 2008.

6. Marple, S. Digital Spectral Analysis with Applications, Prentice Hall, Englewood Cliffs, NJ1987.

7. Meyer, M., M. Desbrun, P. Schröder, and A. Barr. Discrete differential-geometry operators for triangulated 2-manifolds. In: Visualization and Mathematics III (Proceedings of VisMath), pp. 35–54, Springer Berlin Heidelberg, 2003.

8. Petronetto, F., A. Paiva, E. S. Helou, D. E. Stewart, and L. G. Nonato. Mesh-free discrete laplace-beltrami operator. Computer Graphics Forum 32:214–226, 2013.

9. Rosenberg, S. The Laplacian on a Riemannian manifold: an introduction to analysis on manifolds. 31, Cambridge University Press, 1997.

10. Rudy, Y. Noninvasive electrocardiographic imaging of arrhythmogenic substrates in humans. Circulation research 112:863–874, 2013.

11. Sanromán-Junquera, M., I. Mora-Jiménez, A. Caamaño-Fernández, A. García-Alberola, and J. Rojo-Álvarez. Influence of normalization on the analysis of electroanatomical maps with manifold harmonics. In: International Conference on Bioinformatics and Biomedical Engineering, volume 9656, pp. 415–425, 2016.

12. Sanromán-Junquera, M., I. Mora-Jiménez, A. García-Alberola, and J. Rojo-Álvarez. Spectral analysis of electroanatomical maps for spatial bandwidth estimation as support to ablation. In: Computing in Cardiology, volume 42, pp. 181–184, 2015.

13. Sanromán-Junquera, M., I. Mora-Jiménez, J. Saiz, C. Tobón, A. García-Alberola, and J. Rojo-Álvarez. Quantitative spectral criteria for cardiac navigation sampling rate using manifold harmonics analysis. In: Computing in Cardiology, volume 39, pp. 357–360, 2012.

14. Stabile, G., M. Scaglione, M. del Greco, R. De Ponti, M. G. Bongiorni, F. Zoppo, E. Soldati, R. Marazzi, M. Marini, F. Gaita *et al.* Reduced fluoroscopy exposure

during ablation of atrial fibrillation using a novel electroanatomical navigation system: a multicentre experience. Europace 14:60–65, 2012.

15. Taubin, G. A signal processing approach to fair surface design. In: Proceedings of 22nd Annual Conference on Computer Graphics and Interactive Techniques, pp. 351–358, 1995.

16. Tobón, C., C. Ruiz-Villa, E. Heidenreich, L. Romero, F. Hornero, and J. Saiz. A three-dimensional human atrial model with fiber orientation. electrograms and arrhythmic activation patterns relationship. PloS one 8:e50883, 2013.

17. Vallet, B. and B. Lévy. Spectral geometry processing with manifold harmonics. Computer Graphics Forum 27:251–260, 2008.

18. Zhang, H., O. van Kaick, and R. Dyer. Spectral mesh processing. Computer Graphics Forum 29:1865–1894, 2010.

19. Zhou, D. and C. J. Burges. High-order regularization on graphs. In: Intl. Workshop on Mining and Learning with Graphs, pp. 1–8, 2008.

List of Figures

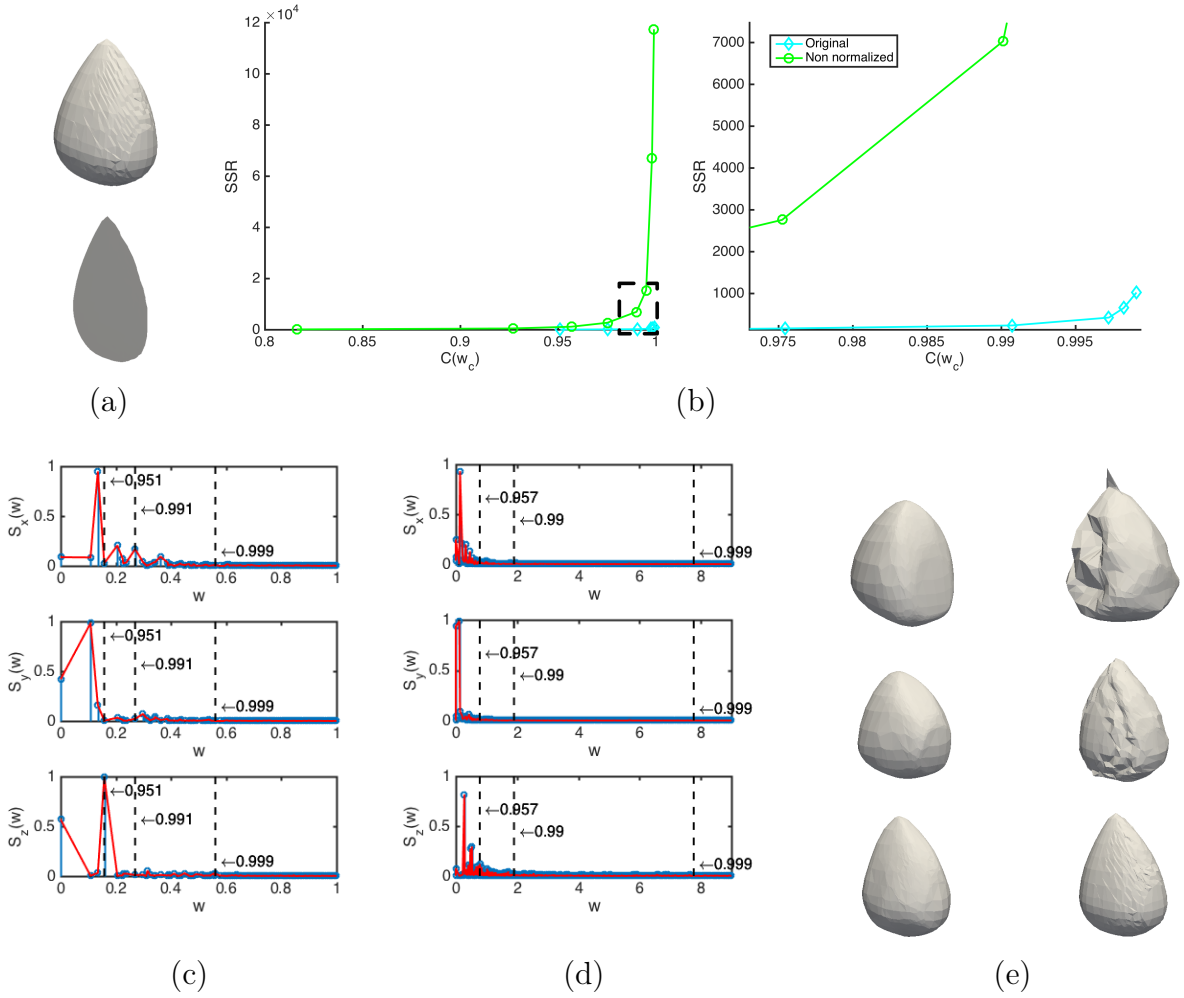

Figure 1: Spectral representation, SSR, and reconstruction of a tear-shaped mesh (a-top) and flatted tear-shaped mesh (a-bottom); (b) SSR of the original tear-shaped mesh and the flatted tear-shaped mesh for different $C(w_c)$; Spectrum of the original (c), and flatted (d) tear-shaped mesh;(e) Reconstructed original (left) and flatted (right) tear-shaped mesh for $C(w_c) \approx 0.95$, $C(w_c) \approx 0.99$, $C(w_c) \approx 0.999$ (from top to bottom). Note that the flatted tear-shaped mesh was resized for comparison purposes.

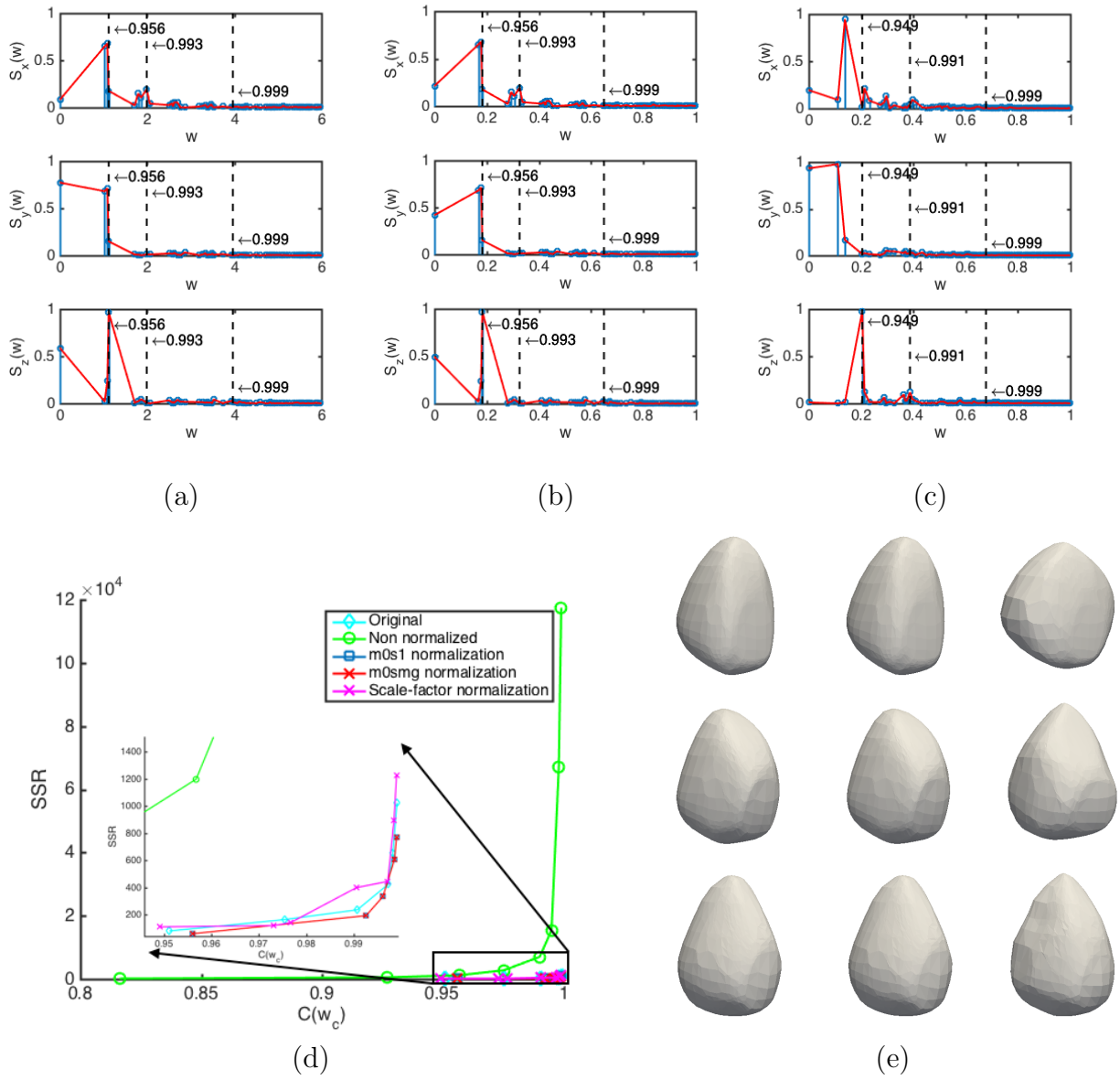

Figure 2: Spectrum of the S1 (a), SMG (b), and SH (c) scaled flatted tear-shape mesh. (d) SSR of original, and the flatted tear-shape mesh with (S1, SMG, and SH) and without scaling for different $C(w_c)$; (e) Reconstruction of the flatted tear-shape mesh for $C(w_c) \approx 0.95$, $C(w_c) \approx 0.99$, $C(w_c) \approx 0.999$ (from top to bottom) using S1, SMG and SH scaling (from left to right).

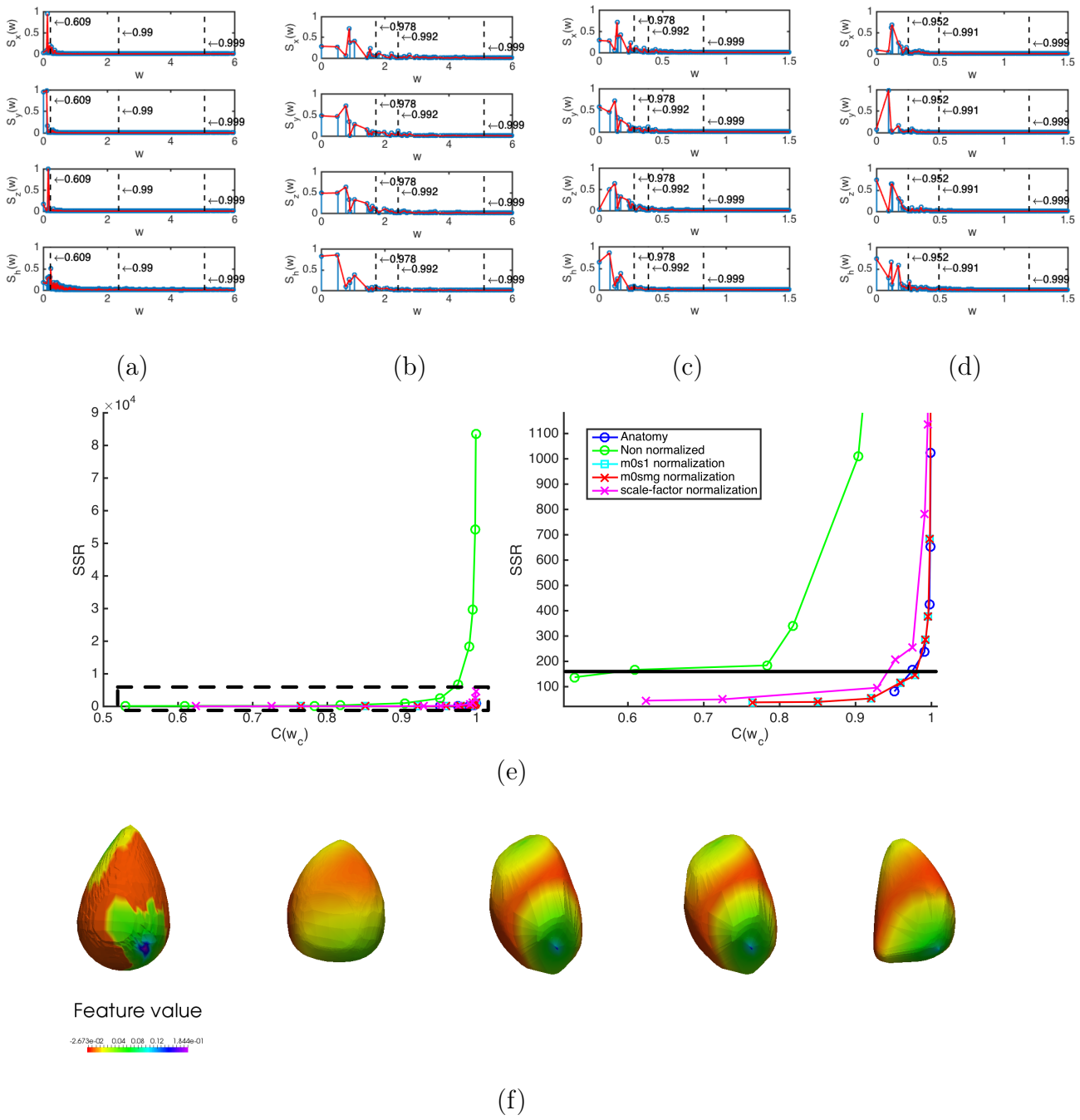

Figure 3: Spectrum of the two-foci EAM without scaling (a), with S1 (b), SMG (c), and sh (d) scaling. (e) SSR of the two-foci EAM with S1, SMG, and SH scaling and without scaling for different $C(w_c)$. The SSR of the anatomy was also included for comparison purposes; (f) Original EAM (left EAM) and reconstructed two-foci EAM (in the black horizontal line) for non-scaled EAM and $C(w_c) = 0.6086$, for S1 and $C(w_c) = 0.978$, for SMG and $C(w_c) = 0.978$, and for SH and $C(w_c) = 0.952$ (from left to right).

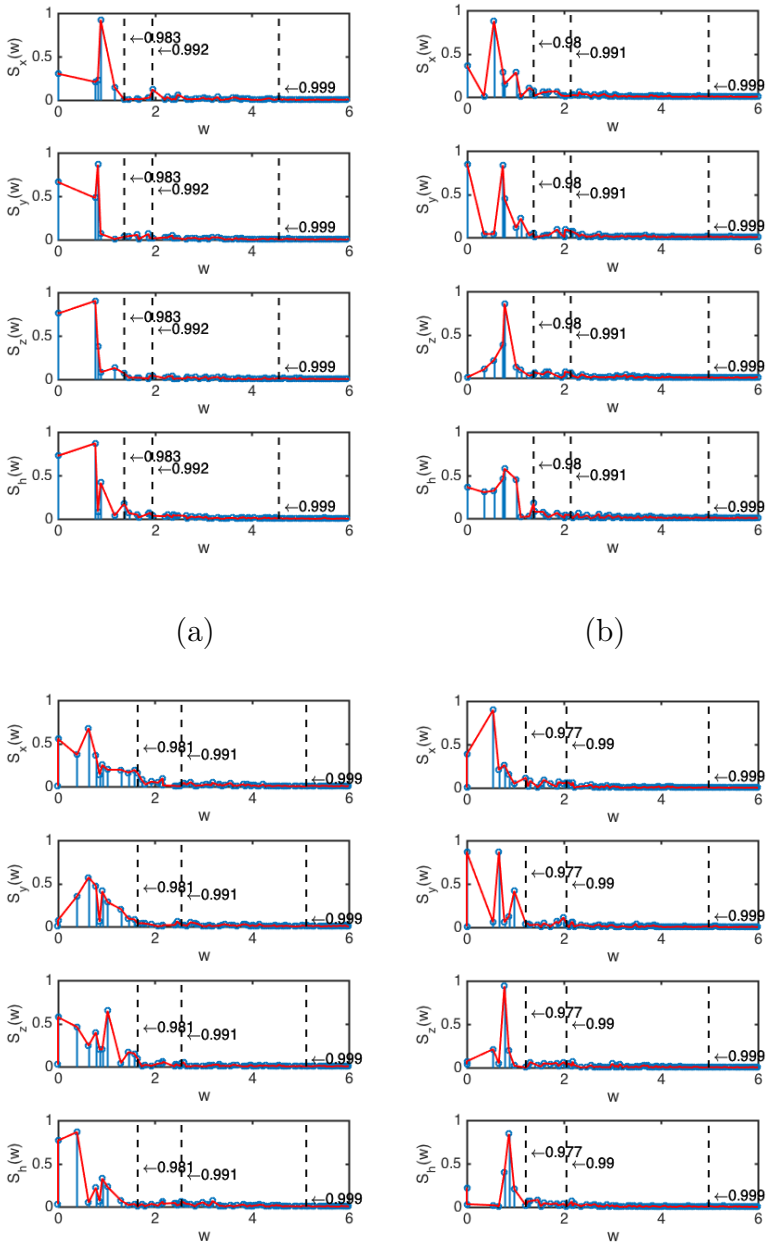

Figure 4: Spectrum of time activation EAMs in the RA (a) and LA (b) during a SR, and in the RA (c) and LA (d) during FL. Vertical lines establish the required w_c to have the $C(w_c) \approx 0.98$, $C(w_c) \approx 0.99$, and $C(w_c) \approx 0.999$.

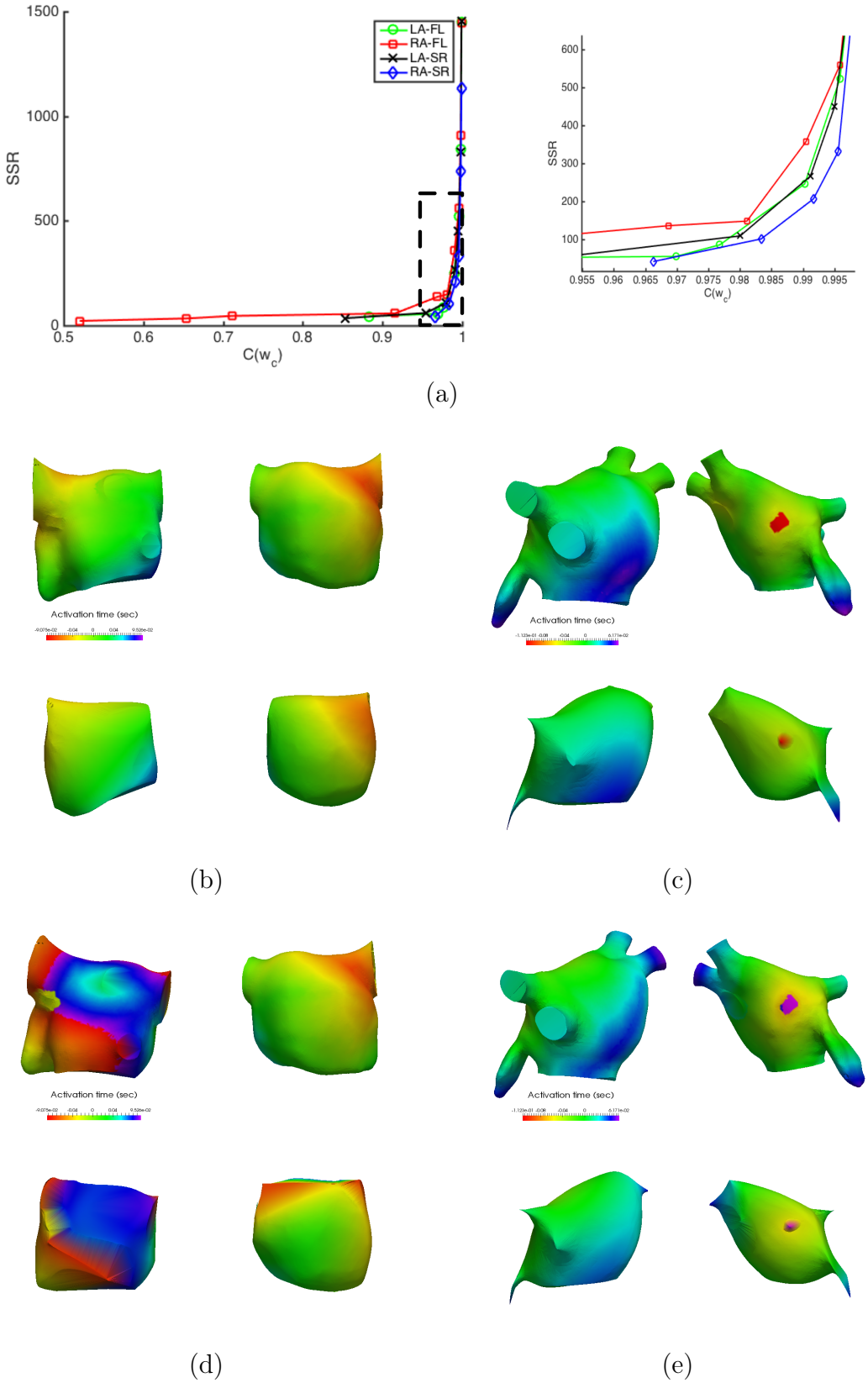

Figure 5: Simulated time activation EAM in RA and LA. (a) SSR for SR and FL in both atria. Reconstructed EAM for $C(w_c) \approx 0.99$ in the RA (b) and LA (c) during SR, and in the RA (d) and LA (e) during FL. Original EAMs (upper panel) and reconstructed EAMs (bottom panel) are shown in both sides.

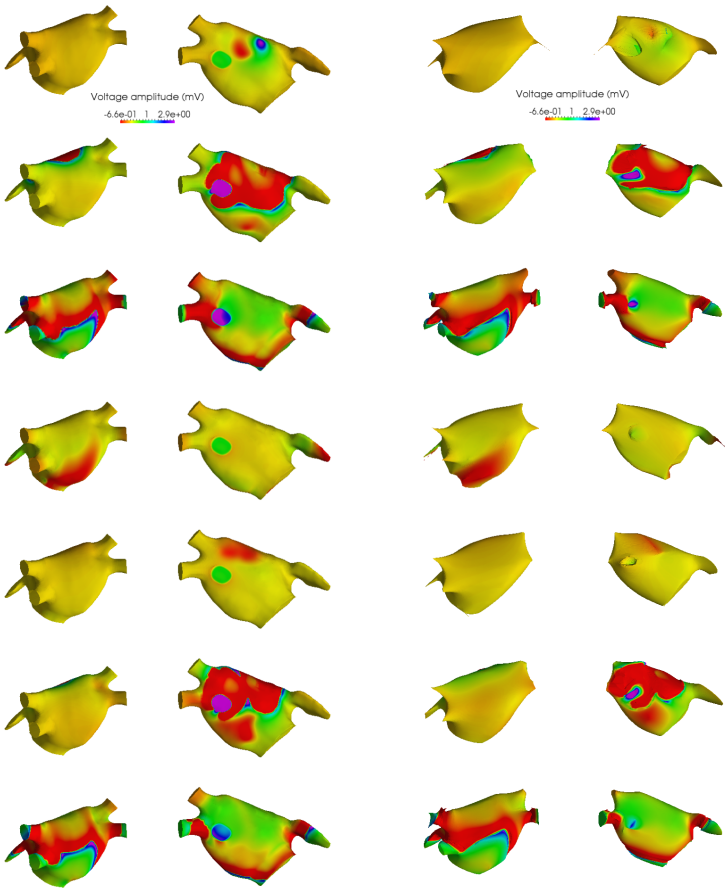

(a)

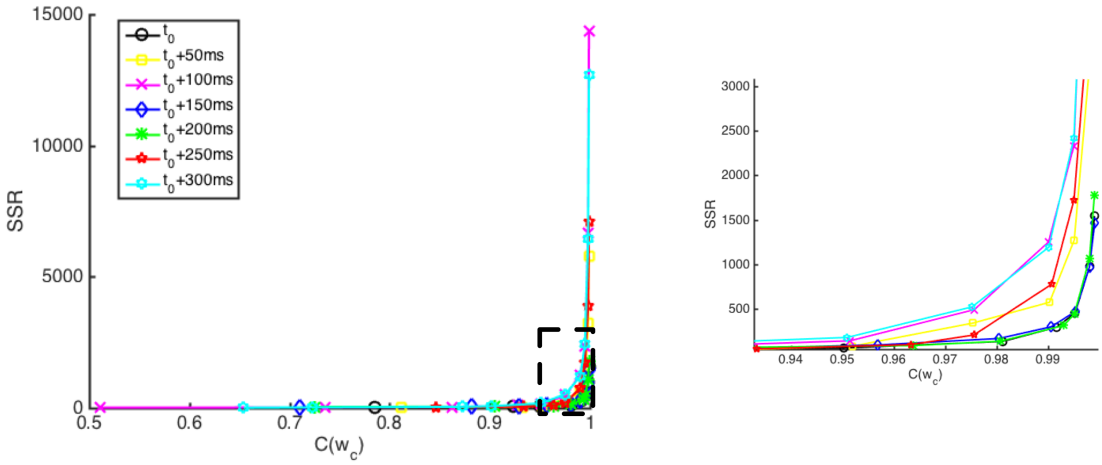

(b)

Figure 6: Original and reconstructed for $C(w_c) \approx 0.99$ temporal series of EAMs for AT in LA (both faces). (c) SSR (and zoom) of temporal series of potential EAMs for AT in LA.

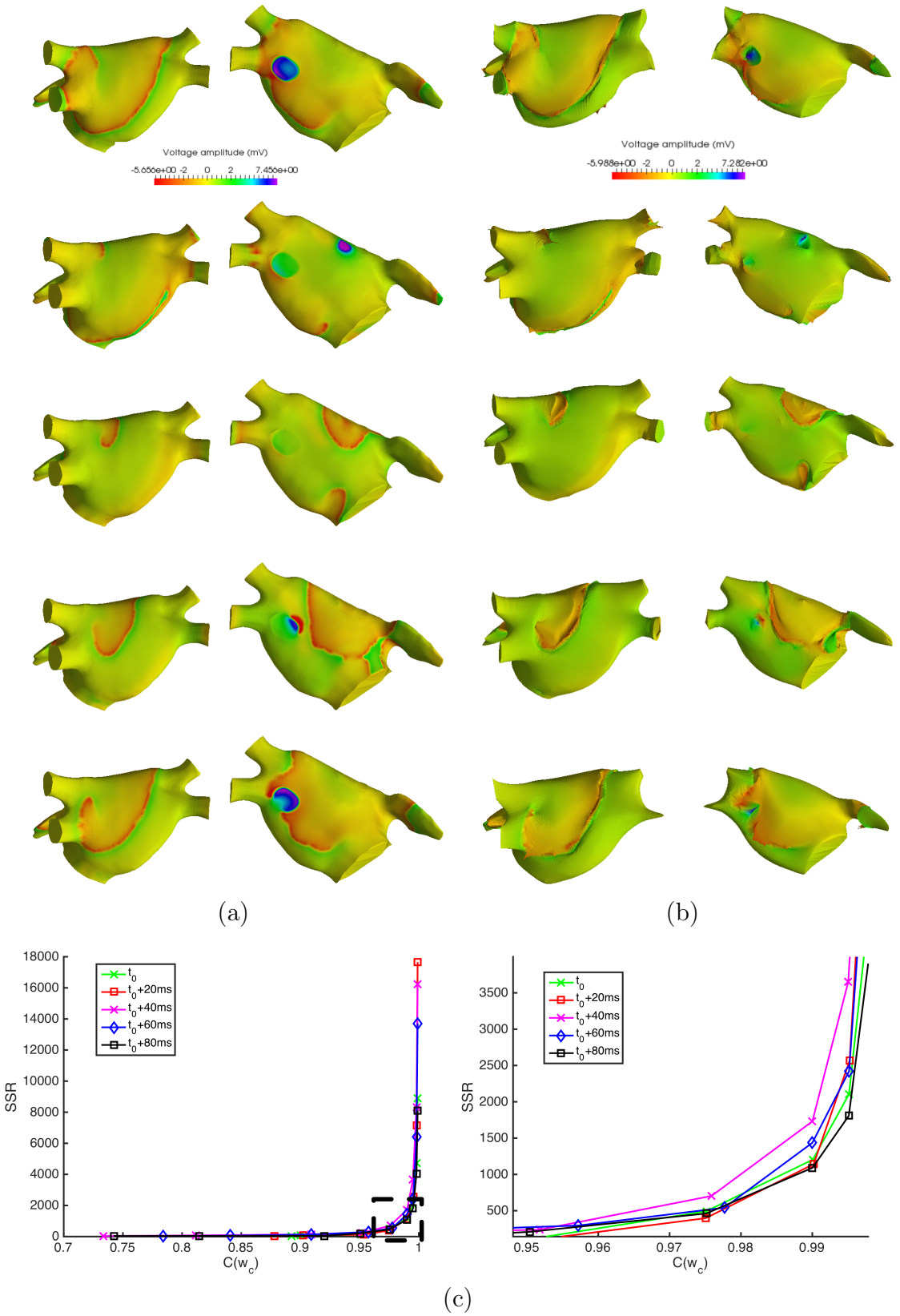

Figure 7: Original (a) and reconstructed for $C(w_c) \approx 0.99$ (b) temporal series of potential EAMs for AF in LA (both faces). (c) SSR (and zoom) of temporal series of potential EAMs for AF in LA.

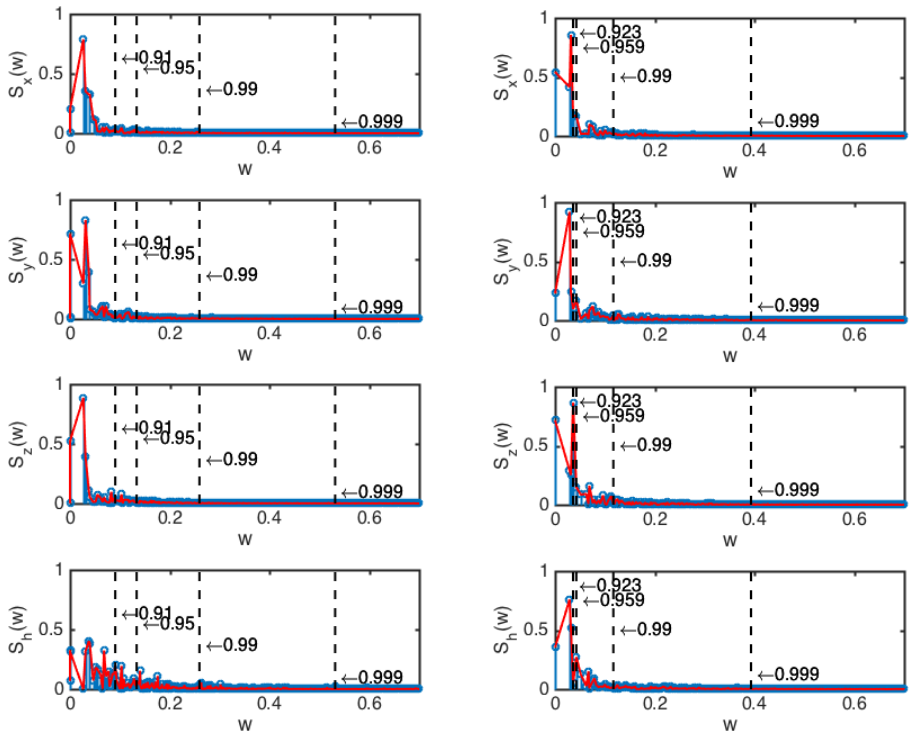

(a) (b)

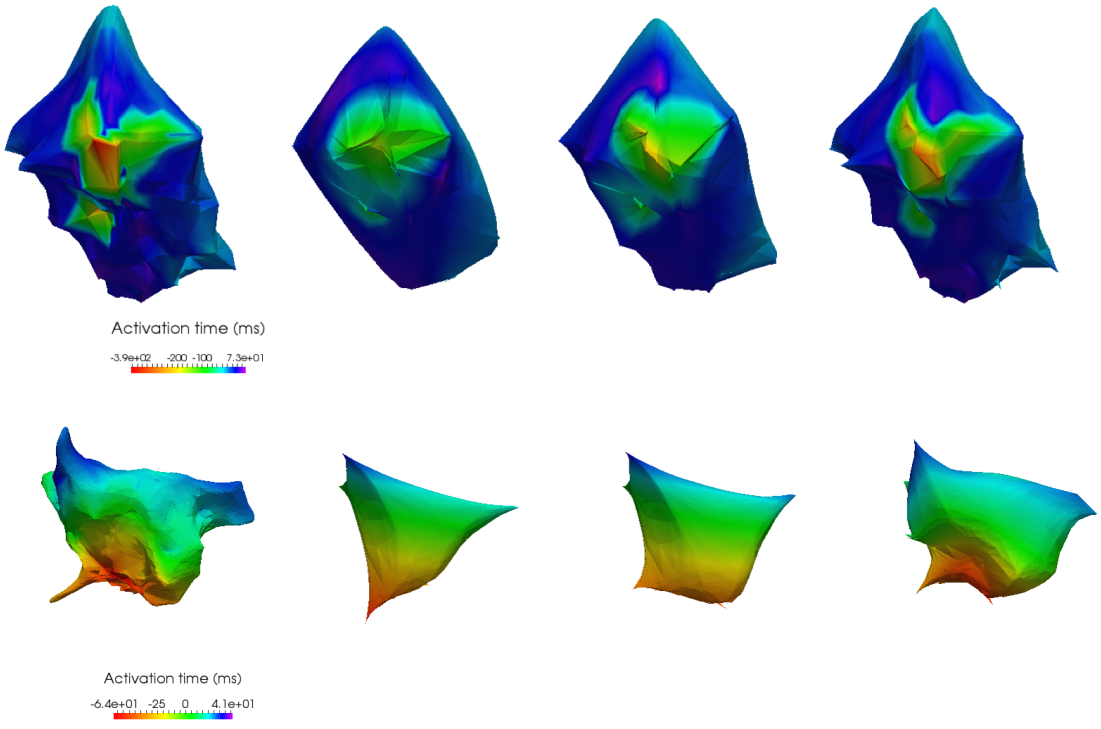

(c)

Figure 8: Spectrum of activation time EAM for LV-1 (a) and LA (b); (c) Original and reconstructed activation time EAM for LV-1 (superior) and LA (inferior) with $C(w_c) \approx 0.9$, $C(w_c) \approx 0.95$, and $C(w_c) \approx 0.99$.

List of Tables

Table 1: SSR for activation time and bipolar EAMs in LA, RV, and LV for a $C(w_c) \approx 0.9$, $C(w_c) \approx 0.95$ and $C(w_c) \approx 0.99$.

EAM	**Cardiac chamber**	$C(w_c)$		
		$\approx$ **0.9**	$\approx$ **0.95**	$\approx$ **0.99**
Time activation	LA	28	39	292
	LV-1	201	436	1647
	LV-2	35	35	318
	LV-3	54	132	512
	LV-4	114	196	1092
	RV-1	27	82	389
	RV-2	19	52	214
	RV-3	21	51	230
	RV-4	43	55	229
Bipolar voltage	LA	64	132	845
	LV-1	35	91	352
	LV-2	32	94	371
	LV-3	71	202	1080
	LV-4	62	124	475
	RV-1	46	65	289
	RV-2	31	65	178
	RV-3	28	82	270
	RV-4	64	83	208